Resources, Conservation & Recycling 182 (2022) 106284

Contents lists available at ScienceDirect

Resources, Conservation & Recycling

journal homepage: www.elsevier.com/locate/resconrec

Full length article

A systematically integrated recycling and upgrading technology for waste crystalline silicon photovoltaic module

Xinhai Xu [a,b], Dengguo Lai [a,*], Wenxuan Wang [a,b], Yin Wang [a,c,**]

[a] CAS Key Laboratory of Urban Pollutant Conversion, Institute of Urban Environment, Chinese Academy of Sciences, Xiamen 361021, China
[b] University of Chinese Academy of Sciences, Beijing 100049, China
[c] Ningbo (Beilun) Zhongke Haixi Industrial Technology Innovation Center, Ningbo 315000, China

ARTICLE INFO

Keywords:
End-of-life photovoltaic module
Waste treatment
Closed-loop recycling
Metal-assisted chemical etching
Black silicon

ABSTRACT

Efficient resource recovery and reutilization are important for overcoming the immense challenges associated with waste photovoltaic module management and the limited raw material supplies, but these processes are significantly impeded by the low recycling efficiency and poor profitability of current technologies. Here, an integrated crystalline silicon cell regeneration technique is proposed by skillfully combining the sequential processes of nondestructive silicon cell recovery, wafer prepurification, one-step ultrapurification and texturing using metal-assisted chemical etching (MACE), and intrasystem reutilization of recovered materials. High-purity and intact silicon wafers are successfully recovered, and various anti-reflection textures including the intriguing dual-scale micro/nano structure are controllably constructed simultaneously by applying a single-step MACE process. The favorable thickness (165 μm), resistivity (1.02–2.28 Ω•cm) and carrier lifetime (1.12–2.47 μs) of the recovered silicon wafers, along with their ultralow reflectivity (5–15%) compared with commercial silicon wafers, make them excellent viable options for high-efficient photovoltaic module production. A rough economic assessment reveals that this integrated strategy presents a lower production cost than that of a conventional recovery process or the price of silicon wafer from industrial production process, and the fully recovered Al frame, tempered glass, Cu ribbons, and high-purity Ag and Al powders can be reused within the system for solar cell regeneration and as catalysts for MACE, resulting in economic viability and high resource sustainability.

1. Introduction

Global warming and the fossil fuel crisis are strong motivators for the development of clean and renewable energies, and the emerging photovoltaic (PV) technology is suggested to be one of the most promising alternatives (Oteng et al., 2021). Numerous studies have been devoted to the improvement of the power conversion efficiency of PV technology (Singh et al., 2021), and a large amount of PV modules have been installed in recent decades (IEA 2000–2040). Accordingly, the resource supply risk for raw materials, including the silicon (Si) and related metals, is increasing due to the large increase in installations, which has already restricted the sustainable development of the PV industry (Guo et al., 2021). In addition, more than 45,000 tons of end-of-life (EoL) PV modules were generated in 2016, and this number will dramatically increase to 1.7–8.0 and 60–78 million tons by 2030 and 2050, respectively, due to the limited service lifetime (25–30 years) of PV modules (Weckend et al., 2016). This large number of EoL PV modules pose new environmental risks and threatens human health (Nain and Kumar, 2021) but provide potential opportunities to the raw material, such as Si and valuable metals (*e.g.*, Ag, Cu, Pb, Al, Sn) (Jung et al., 2016; Chen et al., 2021). Therefore, developing technologies to recycle waste PV modules is imperative.

Recovery and reutilization is one of the most attractive strategies to offset the environmental impact and convert waste PV modules into sustainable resources for the PV industry (Farrell et al., 2019; Heath et al., 2020). Therefore, many efforts have been focused on resource recovery from EoL PV modules, especially the recovery of crystalline Si (c-Si) from c-Si-based PV modules, which dominate the major market share (Song et al., 2021). Currently, some methods, such as chemical dissolution (Kim and Lee, 2012) and thermal decomposition (Tammaro et al., 2015), are proposed to remove the adhesive ethylene-vinyl acetate (EVA) that remains after separating the valuable Al frame from the PV

---

* Corresponding author
** Corresponding author
E-mail addresses: dglai@iue.ac.cn (D. Lai), yinwang@iue.ac.cn (Y. Wang).

https://doi.org/10.1016/j.resconrec.2022.106284
Received 9 December 2021; Received in revised form 9 February 2022; Accepted 8 March 2022

module; thus, tempered glass, Si cells and Cu ribbons can be further recovered. Subsequently, solar grade Si can be reclaimed followed by a chemical etching purification process and reinjected as raw materials for solar cell manufacturing, which contributes to the circular economy. However, Si is usually recovered in the form of fragments or powders, which can only be reused for Si ingot production, inducing high economic and environmental costs. In other words, such recovery methods result in insufficient profitability to maintain the process sustainability, which necessitates seeking a cost-effective, sustainable and benign option. Methods to recover intact Si wafers with direct reuse features for new solar cells refabrication in commercial PV module production line have thus been proposed as an ideal recycling mode (Xu et al., 2021; Deng et al., 2019). Skipping the process of Si ingot production and wafer cutting can save approximately 40% of the cost of PV module production (Liu et al., 2019). Nonetheless, there is still a major challenge for the current technologies: regenerated solar cells from recovered Si wafers tend to exhibit a decreased conversion efficiency (Shin et al., 2017; J.K. Lee et al., 2018), which is not acceptable for the current competitive PV market. Therefore, developing a novel technology that combines nondestructive Si wafer recovery and power conversion efficiency upgrading is of critical importance to this ideal mode but is still challenging.

The power conversion efficiency of Si solar cells is mainly determined by their electrical and optical properties, including the quality of the Si wafers (*e.g.*, intrinsic purity, thickness), the metal electrodes, surface passivation, and the light-trapping ability of the surface structure (Ye et al., 2014). For nondestructively recovered Si wafers, it is difficult to enhance electrical properties by improving their intrinsic purity unless they are fused to reproduce the Si ingot. In addition, impurities on the reclaimed Si cell surface should be removed by chemical etching to obtain pure Si wafers. This process is traditionally vigorous and uncontrollable, easily leading to a sharp decline in wafer thickness (Jung et al., 2016; Kang et al., 2012; Klugmann-Radziemska et al., 2010; Wang et al., 2012; Huang and Tao, 2015; Huang et al., 2017). Consequently, a regenerated solar cell usually exhibits relatively low power conversion efficiency, despite the newly processed metal electrodes and surface passivation (J.K. Lee et al., 2018). In contrast, modifying the recovered Si wafers with a surface texture featuring excellent light-trapping capability is a smart way to achieve comparable or even higher power conversion efficiency than those of new wafers. Si wafers with low reflectivity, named black Si (B-Si), can be easily obtained through surface texturing (Oh et al., 2012; Savin et al., 2015; Liu et al., 2014; Peng et al., 2010). Among B-Si fabrication methods, the metal-assisted chemical etching (MACE) method has attracted widespread attention since it is rapid, simple and controllable, and it fits the current commercial production line (Yhc et al., 2020; Huo et al., 2020). In particular, MACE is a top-down wet chemical etching approach to texturing microscale or nanoscale structures, such as pyramids (Wang et al., 2014; Cao et al., 2016), nanowires (Lin et al., 2019; Chang and Sakdinawat, 2014), and nanoporous Si (Wang et al., 2018; Yuan et al., 2009), in the presence of metal catalysts (e.g., Au and Ag nanoparticles or film), oxidative agents (*e.g.*, H_2O_2, $KMnO_4$, $K_2Cr_2O_7$) and HF. Additionally, a more complex micro/nano composite texture can also be formed using multistep etching processes (Ye et al., 2014; Fang et al., 2015; Wilshaw et al., 2017). All of the above surface structuring methods produce excellent light-trapping ability with low reflectivity, thus contributing to a higher power conversion efficiency. If the MACE method is applied to construct a satisfactory texture for the reclaimed Si wafers, the performance of these wafers can be at least comparable to that of new wafers. However, to the best of our knowledge, this endeavor has not yet been explored.

Building on our newly developed solvothermal swelling coupled with thermal decomposition (SSTD) method (Xu et al., 2021), a novel technology for EoL c-Si PV module recycling and upgrading is proposed for the first time, which integrates an SSTD process for nondestructive Si cell recovery, a sequential acid etching for Si wafer prepurification, a newly extended MACE method for ultrapurification and simultaneous ultralow reflectivity surface texture fabrication, and intrasystem reuse of reclaimed materials. Through this technology, desirable and highly pure Si wafers with intact structure, minimally reduced thickness and excellent light-trapping ability ($R = 5$–15%) are successfully obtained. The properties of the reclaimed Si wafers are characterized and evaluated for new solar cell manufacturing and packaging, which encourages regenerated solar cells with higher power conversion efficiency than that of new commercial solar cells. In addition, this technology shows remarkable advantages in reducing production costs and exhibits closed-loop recycling by fully recovering the tempered glass, Al frame, Cu ribbons and even the highly pure Al and Ag powders from the PV modules for intrasystem reutilization, making the process economically viable and sustainable.

2. Experimental section

2.1. Experimental procedure

The commercial multicrystalline Si (mc-Si) module, including an Al frame, tempered glass, two EVA layers, Si cells (156 mm × 156 mm, *p*-type), Cu ribbons, and a backsheet, as shown in Fig. 1a, was used in this study. In the PV module, Si cell is the core component for photoelectric conversion and is consisted of Ag electrode, anti-reflection coating (ARC), *n*-type Si, *p*-type Si, Al back surface field (BSF), Al-Si alloy and Al electrode (Fig. 1b).

Given the structure of the PV module and Si cell, a systematically integrated process was proposed here for recycling and upgrading the EoL c-Si-based PV module. As illustrated in Fig. 1c, the Al frame was first separated mechanically from the spent c-Si PV module obtained from the PV power station. The Si cells were then recovered nondestructively from the remaining PV module via the SSTD method, which was reported in our previous study (Xu et al., 2021). By demonstrating that pressure derived from the gas that is generated from EVA decomposition and trapped between the Si cells and the tempered glass during thermal treatment was responsible for Si cell damage, we suggested swelling the EVA in hot and pressurized organic vapors to convert the dense structure of the EVA into a loose structure to form a gas release channel before thermal treatment. Specifically, the swelling temperature was 190 °C, the processing duration was 2 h, the organic solvents was a mixture of toluene (0.2 M) and ethanol (0.2 M) and the pressure was kept within 1.2–1.4 MPa by measurement; the following thermal decomposition was conducted at 500 °C for 0.5 h. Consequently, 86.11% of Si cells in a commercial PV module can be reclaimed without any damage, which was approximately an order of magnitude higher than that of a direct thermal decomposition method, suggesting that the SSTD process is a feasible, facile and controllable method for layer separation and considerable nondestructive resource recovery from EoL c-Si PV modules.

The each nondestructively recovered Si cell was then immersed in 3.5 L HCl, HNO_3 and HF solution to remove Al electrode, Ag electrode and ARC sequentially. Different acid concentration, immersion time and temperature were used to select an optimal impurities removal condition. After that, the remaining Si cell was etched in a 3.5 L solution, containing various concentrations of $Cu(NO_3)_2$, $AgNO_3$, HF and H_2O_2 for 5 min at room temperature for ultrapurification and simultaneous surface structure fabrication. The residual metal nanoparticles were then completely removed using HNO_3 (30 wt.%) ultrasonically at room temperature for 15 min and a mixture of $HCl/H_2O_2/H_2O$ (1/1/6) at 80 °C for 20 min. Afterwards, a post-treatment by dipping the Si wafers in a mixed solution (3.5 L), containing 0.2 M KOH and 10 vol% isopropyl alcohol (IPA) was applied to modify the rough surface structure at 50 °C for 90 s. The obtained Si wafers were finally rinsed with ultrapure water and dried by nitrogen.

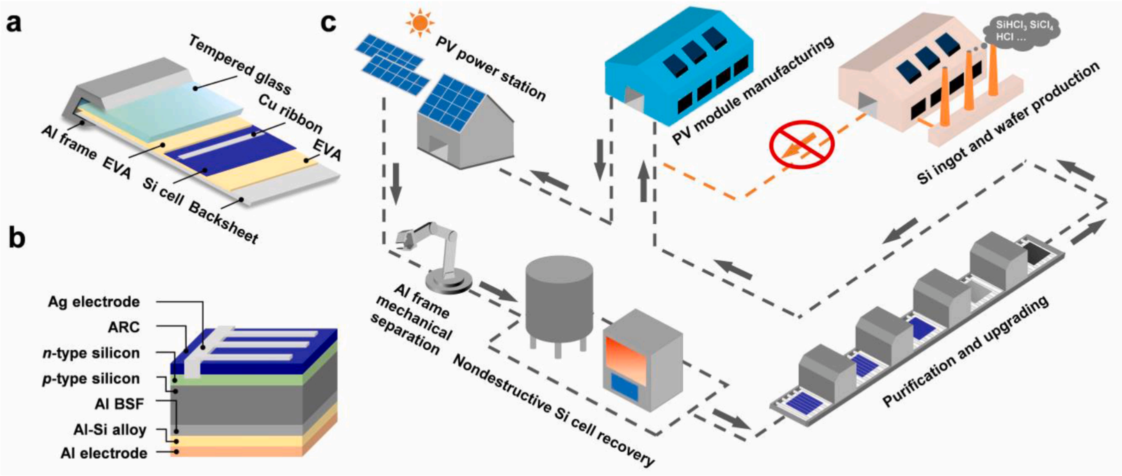

Fig. 1. Schematic illustration of the typical structure of a (a) c-Si-based PV module, (b) Si cell, and (c) the integrated process for EoL c-Si-based PV module recycling and upgrading.

2.2. Analysis and characterization

To evaluate the removal efficiencies of the Al and Ag electrodes, the metal concentrations in the HCl and HNO_3 solutions were measured by inductively coupled plasma-optical emission spectrometry (ICP-OES, Optima 7000DV, PerkinElmer, USA). The surface texture structures and elemental distributions of the recovered Si cells and wafers were analyzed by scanning electron microscopy equipped with energy dispersive spectrometry (SEM-EDS, S-4800, HITACHI, Japan) and X-ray photoelectron spectroscopy (XPS, ESCALAB 250Xi, Thermo Fisher, USA). The reflectivity of the Si wafers was evaluated by a UV–VIS-NIR spectrometer (UV3600, Shimadzu, Japan), and the average reflectivity was calculated with Eq. (1).

$$\overline{R} = \frac{\int_{300nm}^{1100nm} R(\lambda)\cdot S(\lambda)\ d\lambda}{\int_{300nm}^{1100nm} S(\lambda) d\lambda} \tag{1}$$

where$R$ is the average reflectivity of the Si wafer from 300 nm to 1100 nm, λ is the wavelength of incident light, *R(λ)* is the measured reflectivity of the Si wafer, and *S(λ)* is the solar flux under standard AM1.5 conditions.

The thickness of the Si cell and wafer was measured by a micrometer (0.001 mm, NSCING). Four-point probes (FT-8100, ROOKO) was used to characterize the resistivity of the recovered Si wafer. The carrier lifetime of the obtained Si wafer was recorded by microwave-based detection of the photoconductivity decay (μ-PCD, WT1000B, Semilab, USA). X-ray diffraction (XRD, X'Pert Pro, PANalytical B.V., Netherlands) and ICP-OES were applied to evaluate the crystal structure, recovery rate and purity of the recovered metal powders.

3. Results and discussion

3.1. Prepurification of nondestructively reclaimed Si cell

Purification was vital for the reutilization of Si wafers after the nondestructive reclamation. According to the composition of Si cells (Fig. 1b), to obtain pure Si wafers, impurities, including the Ag electrode, ARC, *n*-type Si, Al BSF, Al-Si alloy and Al electrode must be clearly eliminated. In the Si cell manufacturing process, ARC is a Si_3N_4 layer that enhances the light-trapping ability of the Si wafer surface, which is fabricated by plasma chemical vapor deposition. A standard *n*-type Si is formed by phosphorus diffusion to induce the photovoltage, and then the produced current outputs through the Ag and Al electrodes, which are constructed by screen printing and sintering at 800 °C (Kumar et al., 2016). Note that the Al BSF and Al-Si alloy layers are formed during the sintering procedure because the Al-Si eutectic temperature (577 °C) is much lower than the sintering temperature (Figure S1, Supplementary Material) (Rauer et al., 2018). In contrast, Ag-Si alloy is difficult to form owing to the higher Ag-Si eutectic temperature of approximately 840 °C.

To remove impurities on reclaimed Si cells, many chemical etching processes for purification have been proposed (Table S1). Generally, alkali (e.g., KOH, NaOH) or/and a mixture of $HF/HNO_3/H_2O$ are consistently used in these methods because only alkali solutions or HF coupled with oxidants can react with Si to remove impurities that are trapped in Si, according to Eq. (2) and 3.

$$Si + 2KOH + H2O \rightarrow K2SiO3 + 2H2 \tag{2}$$

$$3Si + 4HNO3 + 18HF \rightarrow 3H2SiF6 + 4NO + 8H2O \tag{3}$$

However, these methods are often vigorous and uncontrollable and are mainly applied to recover broken Si wafers or powders for ingot production, where the thicknesses of the recovered wafers or the Si recovery rate is not a critical factor. In other words, the recovery rate of Si is usually sacrificed to improve the purity of the final Si product by overetching of Si. Unfortunately, these methods are not applicable to intact Si wafer purification because the thickness of the Si wafer is critically important for the Si cell power conversion efficiency and the wafer thickness should be at least 160–170 μm before texturing process (Fraunhofer Institute for Solar Energy Systems 2021). Moreover, it has been found that the pure Si wafers obtained by the abovementioned methods usually exhibit a high reflectivity of over 30% (Figure S2). In this case, the texturing process to form a light-trapping structure becomes necessary before Si cell regeneration, which leads to further thickness reduction in the reclaimed Si wafers. Therefore, converting the reclaimed intact Si cell into a viable Si wafer for new cell fabrication still presents a nontrivial challenge.

A mild sequential etching process without alkali and $HF/HNO_3/H_2O$ was employed here to prepurify the reclaimed Si cells, as shown in Fig. 2a. The first etching step was conducted with HCl to remove the Al electrode at room temperature, and the removal efficiency increased with the concentration of HCl (Fig. 2b). Considering the volatility of concentrated HCl, a moderate concentration of 18–24 wt.% was selected, which can completely dissolve the Al electrode in 10–15 min. Then, the obtained Si cell was immersed in a HNO_3 solution to remove the Ag electrode. As illustrated in Fig. 2c, the Ag removal efficiency was strongly dependent on the HNO_3 concentration, presenting an extremely low reaction rate as the HNO_3 concentration decreased below 20 wt.% at 40 °C. To achieve efficient dissolution and to avoid the risks associated with concentrated HNO_3, the effect of temperature on Ag electrode

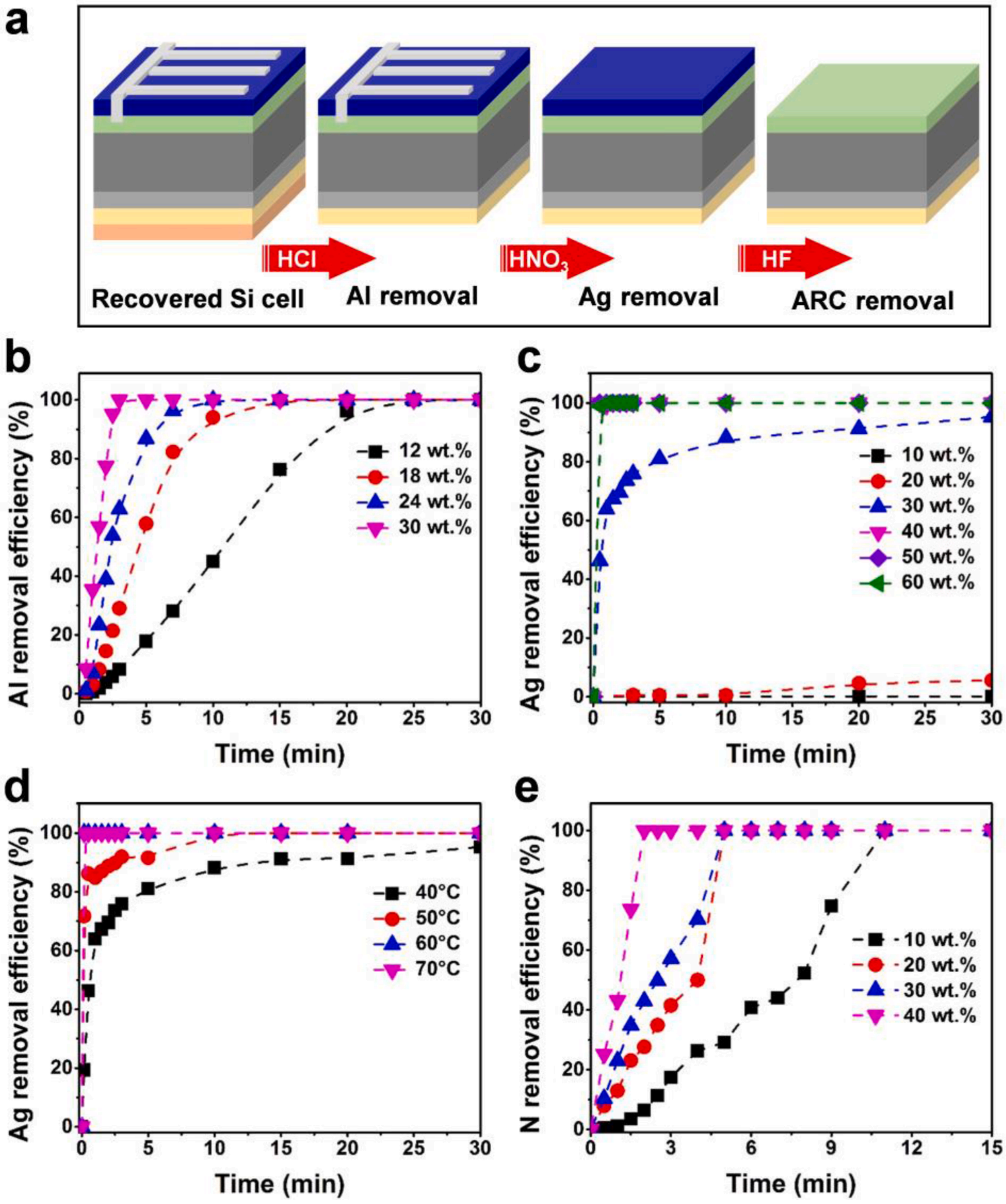

Fig. 2. (a) Flowchart of the sequential etching process. (b) Effect of HCl concentration on Al electrode removal at room temperature. (c) Effect of HNO_3 concentration on Ag electrode removal at 40 °C. (d) Effect of temperature on Ag electrode removal with a HNO_3 concentration of 30 wt.%. (e) Effect of HF concentration on ARC removal at room temperature.

removal was investigated with a relatively low HNO_3 concentration of 30 wt.% Fig. 2.d shows the result and suggests that complete Ag removal could be achieved in 10 min with a slight temperature increase to 50 °C, which might be the preferred condition. After the elimination of metal electrodes, HF was used to remove the ARC layer, and the effect of different concentrations of HF on the removal efficiency is shown in Fig. 2e, indicating a positive correlation. Similarly, taking the volatility of concentrated HF into account, relatively low concentration of 20–30 wt.%, could be optimal, successfully removing ARC in 5 min at room temperature.

Fig. 3a shows photographs of a Si cell reclaimed by the SSTD process and the prepurified Si wafer, labeled as PP-wafer. The disappearance of the metal wires and blue coating suggested the successful removal of the Ag electrode, Al electrode and ARC. In addition, it should be noted that the two sides of the PP-wafer presented different brightness, which can be explained by the surface structure. In the Si cell manufacturing process, one of the essential steps is preparing a textured surface on the front side and a polished surface on the back side to improve light-trapping ability. According to the SEM image of the PP-wafer (Fig. 3b), the original micron-sized texture on the front side and the polished surface on the back side were not destroyed by the sequential acid etching process, thereby resulting in different brightness. In other words, this prepurification method possessed a high recovery rate for Si because almost no Si corrosion occurred during the process.

To verify the purity of the obtained PP-wafer, elemental analysis was performed using EDS and XPS Fig. 3.c shows the elemental content and

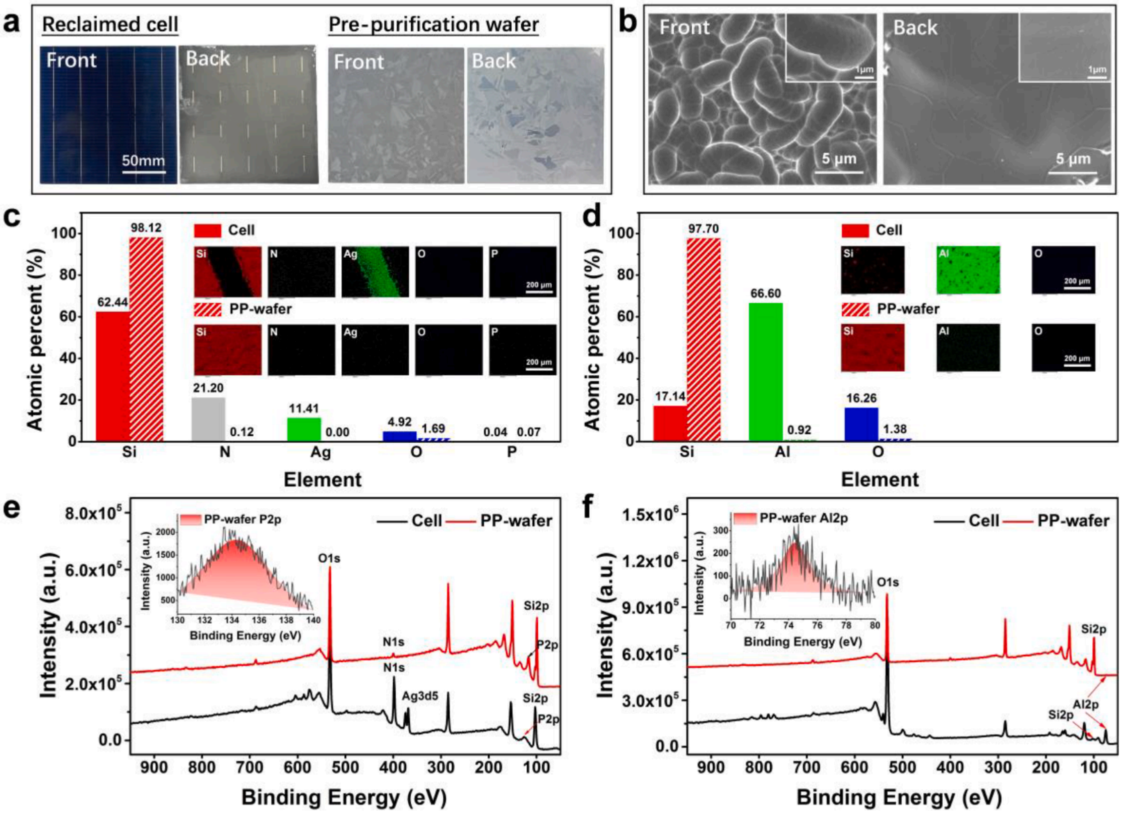

Fig. 3. (a) Photographs of reclaimed Si cells and wafers after prepurification. (b) SEM images of Si wafers after prepurification. (c) EDS analysis and mapping images of the front side of the reclaimed Si cells and wafers after prepurification. (d) EDS analysis and mapping images of the back side of the reclaimed Si cells and wafers after prepurification. (e) XPS analysis of the front side of the reclaimed Si cells and wafers after prepurification. (f) XPS analysis of the back side of the reclaimed Si cells and wafers after prepurification.

distribution on the front side of the reclaimed Si cell and PP-wafer, clearly revealing the successful removal of the Ag electrode and ARC. However, minute amounts of P (0.07%) were found on the front side of the PP-wafer, even higher than that on the reclaimed Si cell, which is consistent with the peak intensity (P 2p at 134.68 eV) in the XPS spectrum (Fig. 3e), probably because the phosphorus diffusion layer was exposed after the ARC removal. In relation to the back side of the PP-wafer, a small amount of Al (0.92%) remained (Fig. 3d) after HCl etching, which is also reflected in XPS observation by a weak peak assigned to Al 2p at 74.88 eV (Fig. 3f). The incomplete elimination of P and Al is unsurprising; unlike the facile reaction between Si_3N_4 and HF (Eq. (4)), Si and HF exhibits extremely low kinetic reaction rate at room temperature unless oxidants such as HNO_3 and $KMnO_4$ are added, as mentioned before (Eq. (3)). In this case, the P doped in Si (phosphorus diffusion layer) could not be removed completely during the ARC removal process in which only HF was present in the etchant. Likewise, despite the reaction of Al and HCl (Eq. (5)), the Al trapped in the Al-Si alloy and BSF layer was difficult to dissolve thoroughly.

$$Si_3N_4+12HF \rightarrow 3SiF4+4NH_3 \qquad (4)$$

$$2Al+6HCl \rightarrow 2AlCl3+3H2 \qquad (5)$$

As a prepurification method, the sequential acid etching process successfully removed most of the impurities on the reclaimed Si cells and avoided the undesired over-etching of Si. Moreover, it is a chemically selective etching process, leaving the Al and Ag dissolved in the HCl and HNO_3 solutions separately, which is conducive to metal recovery and will be discussed later. Of course, the incomplete removal of P and Al still have negative impacts during the solar cell manufacturing using the recovered Si wafers. On the one hand, the Si wafer with residual P after p-n junction preparation tended to form a heavy doping, which would lead to the bond contraction, lattice deformation and surface recombination of photogenerated carriers, hence decreasing the power conversion efficiency. On the other, the metal Al impurity not only introduced many recombination centers, but also polluted the whole solar cell manufacturing system due to the volatilization of Al during high temperature phosphorus diffusion process. Therefore, a further complete purification treatment is required to gain a high-purity Si wafer.

3.2. One-step ultrapurification and upgrading of PP-wafer

To simultaneously ensure purity and maintain thickness, the MACE method was utilized here for further treatment of the PP-wafer, combining the complete impurity removal and anti-reflection texture fabrication processes into a single step. Excessive loss of the resultant high-purity Si wafer could be avoided due to the omission of re-etching to form a surface texture during the Si cell regeneration process. More importantly, various controllable surface structures can be fabricated by the MACE method, exhibiting much lower reflectivity than that by conventional texturing methods, thereby upgrading the reclaimed Si wafers.

Since no endeavor has been made to extend MACE for the treatment of recovered Si wafers previously containing impurities, the process feasibility was demonstrated, and the texture regulation of PP-wafer by MACE was first investigated in this work with the most commonly used metal catalysts, Cu^{2+} and Ag^{+}. As a result, different structures, including a dual-scale micro/nano texture (DMN), nanowires texture, nanoporous texture and inverted rectangular pyramidal structure, were fabricated on the PP-wafers by adjusting the concentration of Cu^{2+} and Ag^{+}, as described in Fig. 4a and 4b. In this experiment, the concentrations of HF and the oxidant (H_2O_2) were kept at 4.6 M and 0.55 M, respectively, and

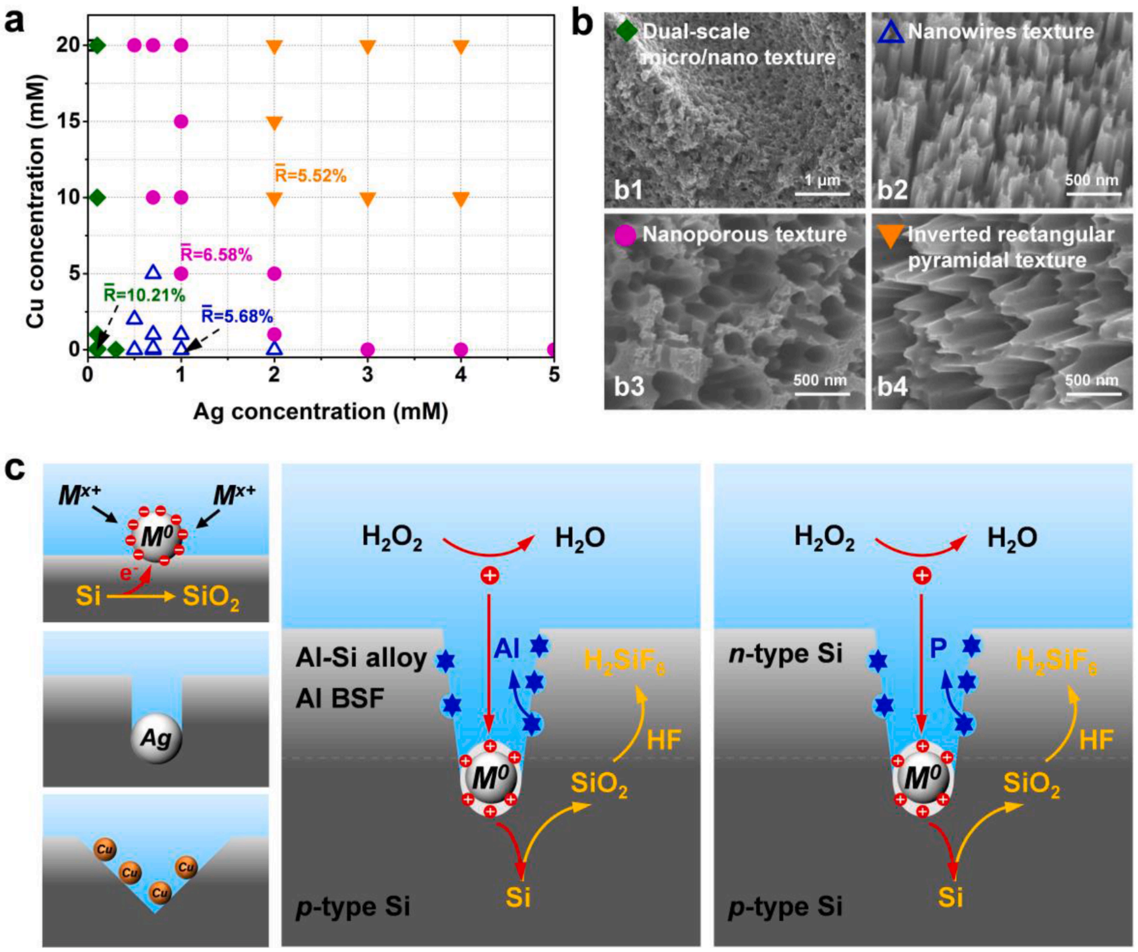

Fig. 4. (a) The evolution of surface texture with different Ag^+ and Cu^{2+} concentrations. (b) SEM images of four typical dual-scale micro/nano texture fabricated with 0.1 mM Ag^+ and 1.0 mM Cu^{2+}, nanowires texture fabricated with 1.0 mM Ag^+, nanoporous texture fabricated with 1.0 mM Ag^+ and 5.0 mM Cu^{2+} and inverted rectangular pyramid fabricated with 2.0 mM Ag^+ and 10 mM Cu^{2+}. (c) Schematic illustration of the MACE and impurity removal processes.

all the Si wafers were etched at room temperature for 5 min. As shown in Fig. 4a, a DMN texture was obtained when the concentration of Ag^+ was lower than 0.3 mM, regardless of the Cu^{2+} concentration. However, the nanostructure built in the DMN texture changed gradually from extremely small rough pores (Fig. 4b1) to larger shallow pits (Figure S3) with increasing Cu^{2+} concentration, which may be determined by the redox potential of the metal catalyst (Chen et al., 2018; Chen et al., 2019). As seen in Fig. 4c, the metal ions in the etchant were reduced to metal nanoparticles and deposited on the Si wafer surface in the MACE process due to the potential difference between Si and the metal catalyst. Then, the higher electronegativity of the metal catalyst induced further electron capture from Si to form a negatively charged surface, thereby attracting metal ions in the etchant by coulombic force and resulting in the growth of metal nanoparticles. Driven by the catalytic activity, the holes generated from H_2O_2 reduction were injected into Si through the formed metal nanoparticles. In this case, the Si in contact with the metal nanoparticles was preferentially oxidized to Si dioxide (SiO_2) and immediately removed by HF. Due to the high redox potential of the Ag^+/Ag couple (0.7796 V), the Ag nanoparticles were endowed with strong electron withdrawal property, which contributed to the faster oxidation and etching of the Si beneath the Ag nanoparticles, hence forming vertical pores with a higher aspect ratio. In contrast, the lower redox potential of the Cu^{2+}/Cu couple (0.345 V) inhibited the electron capture ability, leading to preferential Cu nanoparticle deposition in the direction of the Si orientation with high free bond density; lateral etching rather than vertical etching was thus encouraged by this anisotropic deposition to fabricate lower ratio pits. Accordingly, in the DMN, the nanostructure of rough pores of extremely small sizes gradually converted to shallow pits because lateral etching became more prominent as the concentration of Cu^{2+} in the etchant increased. When the etchant was equipped with a slightly high Ag^+ concentration and low Cu^{2+} concentration, a nanowires texture was obtained (Fig. 4b2). It is reasonable to assume that the reinforced and vertical etching due to the Ag^+ concentration increase dominated the texturing process, causing the formation of the nanowires texture and the disappearance of the original micron-sized texture. As the concentration of Ag^+ or Cu^{2+} was further increased individually, the original micron-sized texture was consistently eliminated, and the surface structure took on a nanoporous texture. In addition, it should be noted that the nanoporous texture presented as nanocylinder pores (Fig. 4b3) owing to the enlarged Ag nanoparticles upon increasing the Ag^+ concentration, while the obtained nanoporous structure via a higher Cu^{2+} concentration developed into inverted pyramids, as illustrated in Figure S4. Due to the simultaneous vertical etching by Ag catalysis and the lateral etching by Cu catalysis, an inverted rectangular pyramidal structure (Fig. 4b4) was fabricated on the PP-wafer after the concentrations of Ag^+ and Cu^{2+} were both increased to a specific level. Correspondingly, the minimum reflectivity of the typical DMN texture, the nanowires texture, the nanoporous texture and the inverted rectangular pyramidal structures was 10.21%, 5.68%, 6.58% and 5.52%, respectively, and all the other reflectivity under different Cu^+ and Ag^+ concentrations can be found in Table S2.

To the best of our knowledge, the MACE method was extended to reclaimed Si wafer treatment here for the first time. By demonstrating the controllable fabrication of various surface textures, it is suggested that MACE can be successfully applied to PP-wafer treatment with the newly established texture regulation techniques. Subsequently, the impurities of P in the *n*-type Si layer and the Al in the Al-Si alloy and Al BSF layer were expected to be removed by the one-step etching process. In Si cell manufacturing, all the *n*-type Si, Al-Si alloy and Al BSF layers are formed through surface diffusion, leaving behind a uniform distribution of P and Al over a shallow depth. With Si dissolution in the MACE process, the trapped P and Al will be exposed and released into the liquid phase. Once etching progresses beyond the shallow depth, the impurities are removed completely, simultaneously obtaining high-purity Si wafers with excellent light-trapping property, as shown in Fig. 4c. Additionally, MACE is a facile and relatively low energy consumption process that can produce the desired performance at room temperature. Nevertheless, purification using a mixture of $HF/HNO_3/H_2O$ usually requires low-temperature condition (even close to 0 °C) due to the vigorous reaction (Qiao et al., 2019), and a higher temperature is essential for alkali treatment to achieve satisfactory impurity removal (Shin et al., 2017; Huang et al., 2017). Furthermore, compared with the $HF/HNO_3/H_2O$ system, H_2O_2 coupled with a metal catalyst was used in MACE to replace HNO_3 as an oxidant, making the etching depth more controllable to ensure an adequate recovered Si wafer thickness.

More interestingly, through a single MACE process, a DMN texture was successfully fabricated on a PP-wafer with 1.0 mM Ag^+ and 5.0 mM Cu^{2+} when the concentrations of HF and H_2O_2 were adjusted to 2.3 M and 0.77 M, respectively, as shown in Fig. 5. It is worth mentioning that the more open nanostructure obtained for the DMN texture here was superior to that presented in Fig. 4b1, which will negatively impact the following passivation and final power conversion efficiency due to its extremely small nanostructure. Two reasons may be responsible for the formation of this DMN texture. Compared with a low Ag^+ concentration ($<$ 0.3 mM), increasing the Ag^+ concentration to 1.0 mM enlarged the catalytic metal nanoparticles, bringing about a more open nanostructure in this DMN texture. On the other hand, the original micron-sized structure was well preserved by changing the dosage of H_2O_2 and HF, despite the same concentrations of metal catalysts as that forming nanoporous texture in Fig. 4b3. According to the MACE process, H_2O_2 was used as an oxidant to oxidize Si, and the formed SiO_2 was then dissolved by HF, thus keeping the etching process continuous. The etchant consisted of a high percentage of oxidant (0.77 M H_2O_2 and 2.3 M HF) here, SiO_2 dissolution was the rate-determining step rather than Si oxidation (Zhao et al., 2020). In this case, the strong oxidation owing to excess H_2O_2 inhibited the Cu^{2+} reductive deposition onto the Si wafer and weakened the lateral etching; moreover, an insufficient HF concentration resulted in a lower etching depth, which jointly prevented the elimination of the original micron-sized texture.

However, Fig. 5a shows that this DMN texture is rough, which has been proven to lead to a lower power conversion efficiency because of the increased recombination centers and poor passivation (Ye et al., 2014). To obtain a more complex and satisfactory surface structure, alkali post-treatment, which is known as a facile method for surface modification and has been widely available for commercial production line (Jwb et al., 2020), was applied, and the related sample was labeled as DMNP-wafer. As a result, the rough structure was successfully converted to a more uniform, smooth and open structure after modification in a mixed solution containing 0.2 M KOH and 10 vol% IPA for 90 s at 50 °C (Fig. 5b).

Fig. 6a-c shows photographs of the obtained PP-wafer, DMN-wafer and DMNP-wafer. Different brightness was obviously presented, which was in agreement with the fabricated surface textures. To prove complete impurity removal, the P on the front and the Al on the back side of the DMNP-wafer were analyzed by XPS (Fig. 6d and 6e). Note that the front side of the PP-wafer displayed a P 2p signal at 134.68 eV, whereas the P 2p peak disappeared on the front side of the DMNP-wafer. Likewise, a peak assigned to Al 2p at 74.88 eV was observed on the back side of the PP-wafer, while the Al content on the back side of the DMNP-

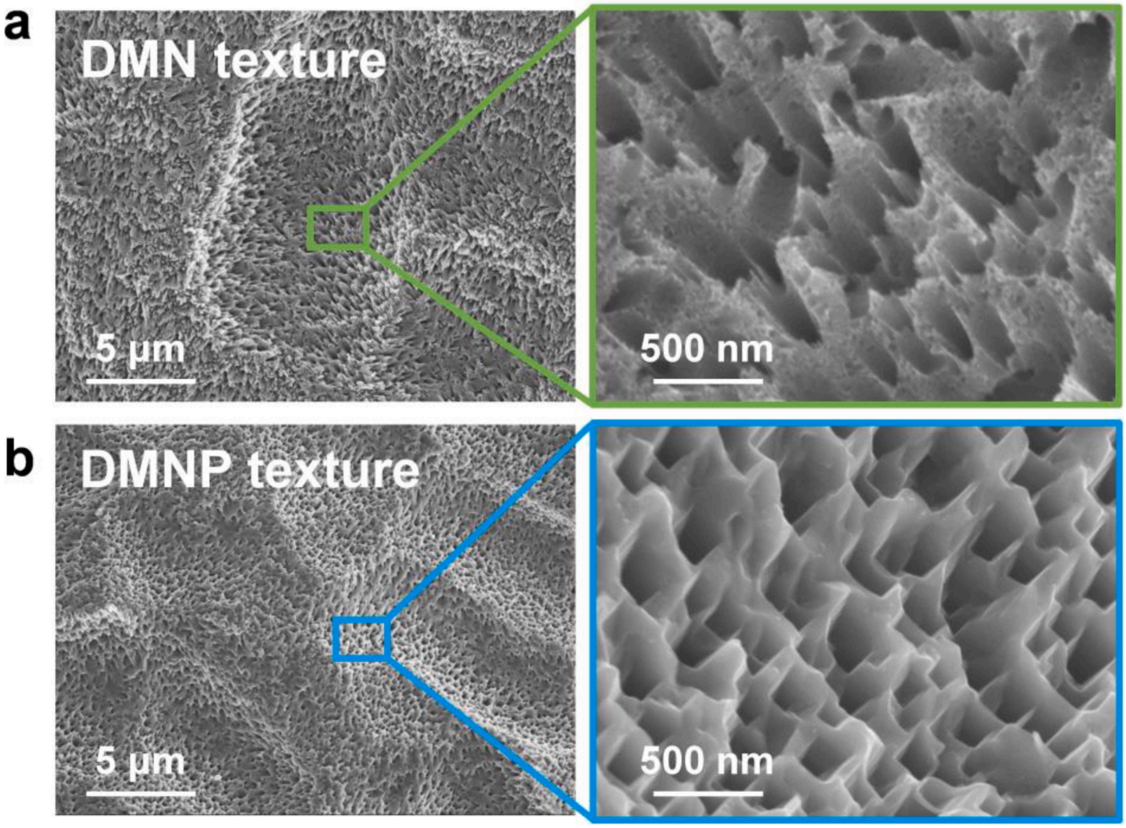

Fig. 5. SEM images of (a) DMN and (b) DMNP textures.

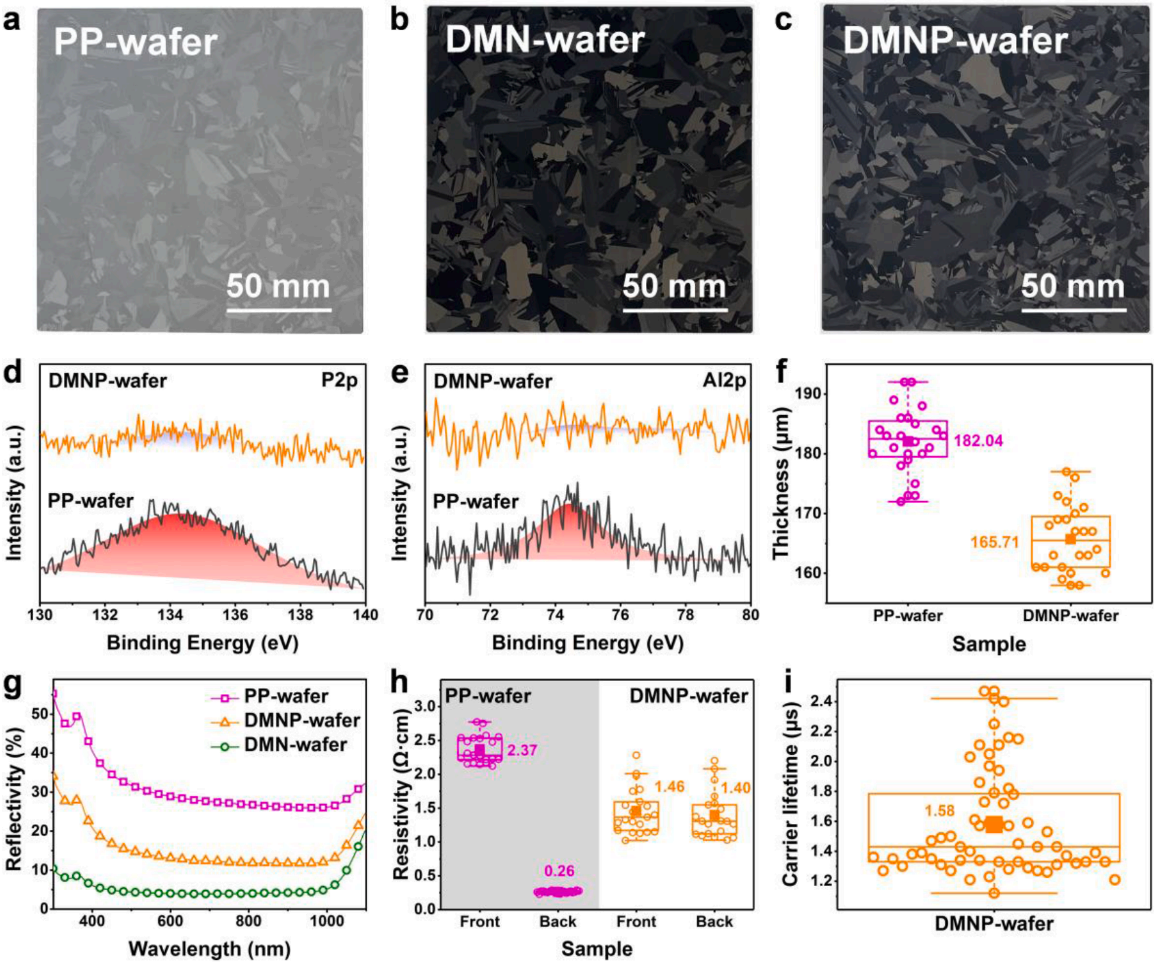

Fig. 6. (a) Photograph of a PP-wafer. (b) Photograph of a DMN-wafer. (c) Photograph of a DMNP-wafer. (d) XPS analysis of the front side of a PP-wafer and DMNP-wafer. (e) XPS analysis of the back side of a PP-wafer and DMNP-wafer. (f) Thickness of PP-wafers and DMNP-wafers. (g) Reflectivity of a PP-wafer, DMN-wafer and DMNP-wafer. (h) Resistivity of PP-wafers and DMNP-wafers. (i) Carrier lifetime of DMNP-wafers.

wafer decreased significantly to below the detection limit. The above results reveal that the ultrapurification of reclaimed Si cells was successfully realized by the MACE process. Moreover, as illustrated in Fig. 6f, the recovered Si wafers presented a relatively low thickness reduction. Specifically, the thickness of the PP-wafer was approximately 182 μm, and the average thickness of the DMNP-wafer was still 165.71 μm after the MACE and the alkali post-treatment processes, which is much thicker than the 140 μm Si wafers reclaimed by the one-step etching process with an acid mixture of 20 wt.% HF and 20 wt.% HNO_3, reported by Lee et al. (J.K. Lee et al., 2018). They further found that the thinner wafer (140 μm) exhibited a lower short circuit current density (J_{sc}), thereby leading to a 0.2% power conversion efficiency decrease in the regenerated solar cell compared with that of a new commercial solar cell, which indicated the importance of wafer thickness and reflected the superiority of the wafer produced in our work. More importantly, a much lower reflectivity was achieved for the reclaimed wafer after the MACE process to enhance light-trapping ability and eliminate retexturing during solar cell regeneration. As shown in Fig. 6g, the average reflectivity of a PP-wafer was 29.23%, which is similar to that of a mc-Si wafer textured by standard commercial technology, suggesting that the micron-sized structure was well preserved after prepurification. With that, a DMN surface texture was successfully fabricated, contributing to a significant $\bar{R}$ decrease to 5.13%. Although alkali post-treatment was then employed to smooth the rough structure, an $\bar{R}$ of 13.99% was obtained, which was still much lower than that of the commercial mc-Si wafer. This lower reflectivity would be beneficial to the power conversion efficiency of solar cells fabricated with these reclaimed Si wafers by increasing J_{sc} according to Eq. (6).

$$J_{sc} = \int_{\lambda_{min}}^{\lambda_{max}} \frac{[1 - R(\lambda)] * I_{AM1.5}(\lambda)}{hc/(q\lambda)} d\lambda \tag{6}$$

where λ is the wavelength of incident light, $R(\lambda)$ is the measured reflectivity of the Si wafer, $I_{AM1.5}(\lambda)$ is the solar spectrum under standard AM1.5 condition, h represents the Planck constant, c is the speed of light and q is the number of electric charge.

In addition, as one of the basic electrical properties, the resistivity of the PP-wafer and DMNP-wafer were measured. Generally, a low doping concentration increases resistivity, and metal diffusion decreases resistivity (Richter et al., 2017). In this case, the deviation in the average resistivity between the front (2.37 Ω•cm) and back sides (0.26 Ω•cm) of the PP-wafer may reveal that some P and Al remained on the surfaces (Fig. 6h). However, similar resistivity for the front and back sides of the DMNP-wafer was observed, with values of 1.46 and 1.40 Ω•cm, respectively, which were similar to those of standard commercial mc-Si wafers. This result further supplied evidence for the successful ultrapurification of Si wafers by the MACE process. Furthermore, the carrier lifetime of the final obtained DMNP-wafer was analyzed (Fig. 6i). As a critical property determining Si wafer quality, a carrier lifetime of 1.12–2.47 μs (1.58 μs on average) of the DMNP-wafer was similar to that of a new mc-Si wafer that was textured with MACE and achieved a high power conversion efficiency. In short, the disadvantages of current recovery and reuse methods mainly lie in low purity and thickness, causing a power conversion efficiency decrease compared with that of new methods. In this work, a highly pure Si wafer was recovered with relatively high thickness, and a series of controllable surface textures were provided to enhance the power conversion efficiency. Unfortunately, the power conversion efficiency of the solar cell regenerated using this recovered Si wafer cannot be provided at this point and is under investigation. Instead, by comparing with some current high-efficient solar cell fabrication technologies (Table S3), it was speculated that a power conversion efficiency improvement could be achieved in our case because the properties of the recovered wafers were comparable to those fabricated by reported MACE methods, which obtained new solar cells with high power conversion efficiency.

3.3. Technical route and economic assessment

To further highlight the superiority of this method, the proposed integrated strategy was compared with two processes: the conventional recovery process (CRP), which focuses on simple raw material recovery from EoL c-Si-based PV modules, and the industrial production process (IPP), which produces Si wafers from silica minerals. As illustrated in Fig. 7a, the integrated technology in this work produced a reusable Si wafer directly from the EoL c-Si PV module instead of silica minerals and successfully converted it into a highly efficient B-Si wafer without increasing the process complexity compared with CRP. In addition, this strategy provided full resource recovery of not only the nondestructive Si wafer, tempered glass, Al frame and Cu ribbons but also the Al_2O_3 and Ag_2O powder from the Al and Ag electrodes on the Si cell. Thanks to the abovementioned prepurification by sequential acid etching, the Al and Ag electrodes were dissolved in HCl and HNO_3 solutions separately, contributing to the recovery of highly pure metal from the etching wastewater without any additional purification methods, such as extraction (Cho et al., 2019) or electrolysis (J.K. Lee et al., 2018). Through simple precipitation and calcination, 95.24% and 94.18% of the Al and Ag at high purities of 98.03% and 99.9% were recovered in the forms of Al_2O_3 (Figure S5a) and Ag_2O (Figure S5b), respectively. Interestingly, in addition to being a potential material for solar cell regeneration, the reclaimed highly pure Ag could be used as a metal catalyst for MACE and could present the same texture regulation as that using commercial reagents (Figure S6), which would reduce noble metal consumption and hazardous waste emissions.

According to the technical routes, a rough economic assessment considering the costs of labor, electricity, reagent, equipment and waste treatment cost was conducted (detailed methods in Figure S7, S8 and Table S4, S5, S6). As shown in Fig. 7b, the one cell production cost of this recycling and upgrading process and CRP was given and compared with the current price of commercial mc-Si wafer from IPP (PVInfoLink 2022). The production cost of the CRP was higher than both the process in this work and current price of commercial mc-Si wafer due to the investment in the processes of Si ingot production and wafer cutting, which are the main energy-consuming processes during wafer manufacturing. In this case, even when the profit of the byproducts (Fig. 7c) were considered, recycling financial subsidies may still be needed to maintain the operation. Interestingly, the process in this work presented a relatively lower production cost than the price of commercial mc-Si wafer, owing to the nondestructively recovered and upgraded B-Si wafers in a short operation time (Dias et al., 2021). Furthermore, the byproducts derived from EoL PV module treatment can add extra profits to the recovery process to offset the production costs or they can be internally used for new solar cell regeneration. As demonstrated by the above results, although the production costs may be underestimated, it can still be speculated that this integrated strategy of highly efficient resource recycling and Si wafer upgrading from the EoL c-Si PV module is economically viable or justifiable for investment.

4. Conclusion

In summary, this work describes a new integrated recycling and upgrading strategy to nondestructively recover Si cells from EoL c-Si PV modules and directly convert them to highly pure Si wafers with ultralow reflectivity via a one-step MACE process for new solar cell manufacturing. The surface texture of the recovered Si wafers by Cu/Ag-assisted chemical etching was regulated, and a series of surface structures, including DMN, nanowires, and nanoporous and inverted rectangular pyramidal textures, were fabricated in a simple, facile and controllable manner. In addition to favorable properties, such as adequate thickness (165 μm), resistivity (1.02–2.28 Ω•cm) and carrier lifetime (1.12–2.47 μs), the obtained Si wafers presented excellent light-trapping ability ($\overline{R} = 5$–15%), endowing the regenerated solar cells with even higher power conversion efficiency than that of new commercial solar cells. Furthermore, this strategy provided a full recovery of the tempered glass, Al frame, Cu ribbons, and highly pure Al and Ag powder from the PV modules to form a closed-loop recycling system. Compared with the current recovery process and industrial production line, this integrated strategy was economically viable due to the upgraded Si

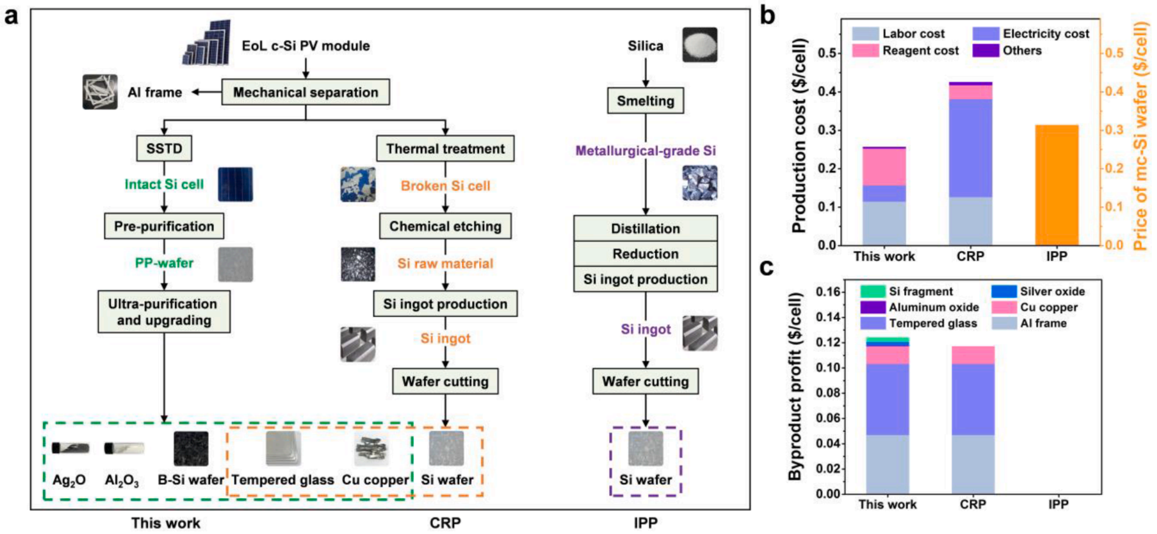

Fig. 7. (a) Schematic illustration of the proposed integrated recycling and upgrading process and conventional recovery process for the EoL c-Si PV module and the commercial production line of a Si wafer from silica mining. (b) Production cost analysis. (c) Byproduct profit analysis.

wafers and full resource recovery for intrasystem reutilization with no process complexity introduced. Therefore, this strategy opens new avenues for resource supply and EoL c-Si PV waste management, contributing to the sustainable development of PV technologies.

CRediT authorship contribution statement

Xinhai Xu: Conceptualization, Data curation, Formal analysis, Investigation, Methodology, Validation, Visualization, Writing – original draft. **Dengguo Lai:** Conceptualization, Formal analysis, Methodology, Resources, Supervision, Writing – review & editing. **Wenxuan Wang:** Data curation, Investigation. **Yin Wang:** Funding acquisition, Project administration, Resources, Supervision, Writing – review & editing.

Declaration of competing interest

The authors declare that they have no known competing financial interests or personal relationships that could have appeared to influence the work reported in this paper.

Acknowledgements

This work is supported by the Technology R & D and Application Demonstration for Sustainable Development of Biomass Waste Recycling in Southeast Asian Countries (No. ANSO—CR-KP-2021–08), National Natural Science Foundation of China (No. 52102120), “Strategic Priority Research Program (A)” of the Chinese Academy of Sciences (No. XDA23030301), the Industry Leading Key Projects of Fujian Province (No. 2019H0056), the Social Development Leading Key Projects of Fujian Province (No. 2021Y0069), CAS Engineering Laboratory for Recycling Technology of Municipal Solid Waste, and the Special Research Assistant Program of the Chinese Academy of Sciences.

Supplementary materials

Supplementary material associated with this article can be found, in the online version, at doi:10.1016/j.resconrec.2022.106284.

References

Oteng, D., Zuo, J., Sharifi, E., 2021. A scientometric review of trends in solar photovoltaic waste management research. Sol. Energy 224, 545–562. https://doi.org/10.1016/j.solener.2021.06.036 https://doi.org/.

Singh, B.P., Goyal, S.K., Kumar, P., 2021. Solar PV cell materials and technologies: analyzing the recent developments. Mater. Today: Proc. 43, 2843–2849. https://doi.org/10.1016/j.matpr.2021.01.003 https://doi.org/.

IEA, Installed power generation capacity in the Stated Policies Scenario, 2000-2040. https://www.iea.org/data-and-statistics/charts/installed-power-generation-capacity-in-the-stated-policies-scenario-2000-2040.

Guo, J., Liu, X., Yu, J., Xu, C., Senthil, R.A., 2021. An overview of the comprehensive utilization of silicon-based solid waste related to PV industry. Resour. Conserv. Recy. 169, 105450 https://doi.org/10.1016/j.resconrec.2021.105450 https://doi.org/.

S. Weckend, A. Wade, G. Heath, End-of-life management: solar photovoltaic panels, 2016. https://www.irena.org/publications/2016/Jun/End-of-life-management-Solar-Photovoltaic-Panels.

Nain, P., Kumar, A., 2021. Understanding metal dissolution from solar photovoltaics in MSW leachate under standard waste characterization conditions for informing end-of-life photovoltaic waste management. Waste Manage. 123, 97–110. https://doi.org/10.1016/j.wasman.2021.01.013 https://doi.org/.

Jung, B., Park, J., Seo, D., Park, N., 2016. Sustainable system for raw-metal recovery from crystalline silicon solar panels: from noble-metal extraction to lead removal. ACS Sustainable Chem. Eng. 4, 4079–4083. https://doi.org/10.1021/acssuschemeng.6b00894 https://doi.org/.

Chen, W., Chen, Y., C, Lee, Cheng, Y., Chueh, Y., 2021. Recovery of valuable materials from the waste crystalline-silicon photovoltaic cell and ribbon. Processes 9, 712. https://doi.org/10.3390/pr9040712 https://doi.org/.

Farrell, C., Osman, A.I., Zhang, X., Murphy, A., Doherty, R., Morgan, K., Rooney, D.W., Harrison, J., Coulter, R., Shen, D., 2019. Assessment of the energy recovery potential of waste Photovoltaic (PV) modules. Sci. Rep. 9, 5267. https://doi.org/10.1038/s41598-019-41762-5 https://doi.org/.

Heath, G.A., Silverman, T.J., Kempe, M., Deceglie, M., Wade, A., 2020. Research and development priorities for silicon photovoltaic module recycling to support a circular economy. Nat. Energy (5), 502–510. https://doi.org/10.1038/s41560-020-0645-2 https://doi.org/.

Song, Q., Zhang, L., Yang, C., Xu, Z., 2021. Novel Electrodeposition method for Cu-In-Cd-Ga sequential separation from waste solar cell: mechanism, application, and environmental impact assessment. Environ. Sci. Technol. 55, 10724–10733. https://doi.org/10.1021/acs.est.1c02496 https://doi.org/.

Kim, Y., Lee, J., 2012. Dissolution of ethylene vinyl acetate in crystalline silicon PV modules using ultrasonic irradiation and organic solvent. Sol. Energy Mate. Sol. Cells 98, 317–322. https://doi.org/10.1016/j.solmat.2011.11.022 https://doi.org/.

Tammaro, M., Rimauro, J., Fiandra, V., Salluzzo, A., 2015. Thermal treatment of waste photovoltaic module for recovery and recycling: experimental assessment of the presence of metals in the gas emissions and in the ashes. Renew. Energy 81, 103–112. https://doi.org/10.1016/j.renene.2015.03.014 https://doi.org/.

Xu, X., Lai, D., Wang, G., Wang, Y., 2021. Nondestructive silicon wafer recovery by a novel method of solvothermal swelling coupled with thermal decomposition. Chem. Eng. J. 418, 129457 https://doi.org/10.1016/j.cej.2021.129457 https://doi.org/.

Deng, R., Chang, N.L., Ouyang, Z., Chong, C.M., 2019. A techno-economic review of silicon photovoltaic module recycling. Renew. Sustain. Energy Rev. 109, 532–550. https://doi.org/10.1016/j.rser.2019.04.020 https://doi.org/.

Liu, Y., Kong, J., Zhuang, Y., Xing, P., Yin, H., Luo, X., 2019. Recycling high purity silicon from solar grade silicon cutting slurry waste by carbothermic reduction in the electric arc furnace. J. Clean. Prod. 224, 709–718. https://doi.org/10.1016/j.jclepro.2019.03.187 https://doi.org/.

Shin, J., Park, J., Park, N., 2017. A method to recycle silicon wafer from end-of-life photovoltaic module and solar panels by using recycled silicon wafers. Sol. Energy Mater. Sol. Cells 162, 1–6. https://doi.org/10.1016/j.solmat.2016.12.038 https://doi.org/.

Lee, J.K., Lee, J.S., Ahn, Y.S., Kang, G.H., Song, H.E., Kang, M.G., Kim, Y.H., Cho, C.H., 2018a. Simple pretreatment processes for successful reclamation and remanufacturing of crystalline silicon solar cells. Prog. Photovoltaics 26, 179–187. https://doi.org/10.1002/pip.2963 https://doi.org/.

Ye, X., Zou, S., Chen, K., Li, J., Su, X., 2014. 18.45%-efficient multi-crystalline silicon solar cells with novel nanoscale pseudo-pyramid texture. Adv. Funct. Mater. 24, 6708–6716. https://doi.org/10.1002/adfm.201401589 https://doi.org/.

Kang, S., Yoo, S., Lee, J., Boo, B., Ryu, H., 2012. Experimental investigations for recycling of silicon and glass from waste photovoltaic modules. Renew. Energy 47, 152–159. https://doi.org/10.1016/j.renene.2012.04.030 https://doi.org/.

Klugmann-Radziemska, E., Ostrowski, P., Drabczyk, K., Panek, P., Szkodo, M., 2010. Experimental validation of crystalline silicon solar cells recycling by thermal and chemical methods. Sol. Energy Mater. Sol. Cells 94, 2275–2282. https://doi.org/10.1016/j.solmat.2010.07.025 https://doi.org/.

Wang, T.Y., Hsiao, J.C., Du, C.H., 2012. Recycling of materials from silicon base solar cell module. In: 38th IEEE Photovoltaic Specialists Conference, pp. 2355–2358. https://doi.org/10.1109/PVSC.2012.6318071 https://doi.org/.

Huang, W.H., Tao, M., 2015. A simple green process to recycle Si from crystalline-Si solar cells. In: 42nd IEEE Photovoltaic Specialist Conference, pp. 1–4. https://doi.org/10.1109/PVSC.2015.7356259 https://doi.org/.

Huang, W.H., Shin, W.J., Wang, L., Sun, W.C., Tao, M., 2017. Strategy and technology to recycle wafer-silicon solar modules. Sol. Energy 144, 22–31. https://doi.org/10.1016/j.solener.2017.01.001 https://doi.org/.

Oh, J., Yuan, H.C., Branz, H.M., 2012. An 18.2%-efficient black-silicon solar cell achieved through control of carrier recombination in nanostructures. Nat. Nanotech. 7, 743–748. https://doi.org/10.1038/nnano.2012.166 https://doi.org/.

Savin, H., Repo, P., Gastrow, G.V., Ortega, P., Calle, E., Garín, M., Alcubilla, R., 2015. Black silicon solar cells with interdigitated back-contacts achieve 22.1% efficiency. Nat. Nanotech. 10, 624–628. https://doi.org/10.1038/nnano.2015.89 https://doi.org/.

Liu, X., Coxon, P.R., Peters, M., Hoex, B., Cole, J.M., Fray, D.J., 2014. Black silicon: fabrication methods, properties and solar energy applications. Energy Environ. Sci. 7, 3223–3263. https://doi.org/10.1039/C4EE01152J https://doi.org/.

Peng, K.Q., Wang, X., Li, L., Wu, X.L., Lee, S.T., 2010. High-performance silicon Nanohole solar cells. J. Am. Chem. Soc. 132, 6872–6873. https://doi.org/10.1021/ja910082y https://doi.org/.

Yhc, A., Btw, A., Sjb, C., 2020. Black-silicon-assisted photovoltaic cells for better conversion efficiencies: a review on recent research and development efforts. Mater. Today Energy 18, 100539. https://doi.org/10.1016/j.mtener.2020.100539 https://doi.org/.

Huo, C., Wang, J., Fu, H., Li, X., Yang, Y., Wang, H., Mateen, A., Farid, G., Peng, K.Q., 2020. Metal-assisted chemical etching of silicon in oxidizing HF solutions: origin, mechanism, development, and black silicon solar cell application. Adv. Funct. Mater. 30, 2005744 https://doi.org/10.1002/adfm.202005744 https://doi.org/.

Wang, Y., Yang, L., Liu, Y., Mei, Z., Chen, W., Li, J., Liang, H., Kuznetsov, A., Xiaolong, D., 2014. Maskless inverted pyramid texturization of silicon. Sci. Rep. 5, 10843. https://doi.org/10.1038/srep10843 https://doi.org/.

Cao, M., Li, S., Deng, J., Li, Y., Ma, W., Zhou, Y., 2016. Texturing a pyramid-like structure on a silicon surface via the synergetic effect of copper and Fe(III) in hydrofluoric acid solution. Appl. Surf. Sci. 372, 36–41. https://doi.org/10.1016/j.apsusc.2016.03.021 https://doi.org/.

Lin, Y.K., Chen, Y.S., Hsueh, C.H., 2019. Combined metal-assisted chemical etching and anisotropic wet etching for anti-reflection inverted pyramidal cavities on dendrite-like textured substrates. Results Phys. 12, 244–249. https://doi.org/10.1016/j.rinp.2018.11.051 https://doi.org/.

Chang, C., Sakdinawat, A., 2014. Ultra-high aspect ratio high-resolution nanofabrication for hard X-ray diffractive optics. Nat. Commun. 5, 4243. https://doi.org/10.1038/ncomms5243 https://doi.org/.

Wang, P., Xiao, S., Jia, R., Sun, H., Dai, X., Su, G., Tao, K., 2018. 18.88%-efficient multi-crystalline silicon solar cells by combining Cu-catalyzed chemical etching and post-treatment process. Sol. Energy 169, 153–158. https://doi.org/10.1016/j.solener.2018.04.049 https://doi.org/.

Yuan, H.C., Yost, V.E., Page, M.R., Stradins, P., Meier, D.L., Branz, H.M., 2009. Efficient black silicon solar cell with a density-graded nanoporous surface: optical properties, performance limitations, and design rules. App. Phys. Lett. 95, 19–1586. https://doi.org/10.1063/1.3231438 https://doi.org/.

Fang, C., Chen, K., Zhang, J., Ye, X., Su, X., 2015. Next-generation multi-crystalline silicon solar cells: diamond-wire sawing, nano-texture and high efficiency. Sol. Energy Mater. Sol. Cells 141, 132–138. https://doi.org/10.1016/j.solmat.2015.05.030 https://doi.org/.

Wilshaw, Peter, Rahman, R., Boden, Tasmiat, Stuart, A., Amirjan, Nawabjan, 2017. Passivation of all-angle black surfaces for silicon solar cells. Sol. Energy Mater. Sol. Cells 160, 444–453. https://doi.org/10.1016/j.solmat.2016.10.044 https://doi.org/.

Kumar, P., Pfeffer, M., Willsch, B., Eibl, O., 2016. Contact formation of front side metallization in p-type, single crystalline Si solar cells: microstructure, temperature dependent series resistance and percolation model. Sol. Energy Mater. Sol. Cells 145, 358–367. https://doi.org/10.1016/j.solmat.2015.10.042 https://doi.org/.

Rauer, M., Schmiga, C., Glatthaar, M., Glunz, S.W., 2018. Quantitative theoretical and experimental analysis of alloying from screen-printed aluminum pastes on silicon surfaces. Sol. Energy Mater. Sol. Cells 176, 295–301. https://doi.org/10.1016/j.solmat.2017.10.010 https://doi.org/.

Fraunhofer Institute for Solar Energy Systems, Photovoltaics report, 2021. https://www.ise.fraunhofer.de/content/dam/ise/de/documents/publications/studies/Photovoltaics-Report.pdf.

Chen, W., Liu, Y., Yang, L., Wu, J., Chen, Q., Zhao, Y., Wang, Y., Du, X., 2018. Difference in anisotropic etching characteristics of alkaline and copper based acid solutions for single-crystalline Si. Sci. Rep. 8, 3408. https://doi.org/10.1038/s41598-018-21877-x https://doi.org/.

Chen, W., Liu, Y., Wu, J., Chen, Q., Zhao, Y., Wang, Y., Du, X., 2019. High-efficient solar cells textured by Cu/Ag-Cocatalyzed chemical etching on diamond wire sawing multicrystalline silicon. ACS Appl. Mater. Inter. 11, 10052–10058. https://doi.org/10.1021/acsami.9b00724 https://doi.org/.

Qiao, F., Liang, Q., Jiang, Y., 2019. Efficient ice-bath texturing route for multi-crystalline silicon solar cell application. Silicon 11, 1611–1615. https://doi.org/10.1007/s12633-018-9982-1 https://doi.org/.

Zhao, Y., Liu, Y., Chen, W., Wu, J., Du, X., 2020. Regulation of surface texturization through copper-assisted chemical etching for silicon solar cells. Sol. Energy 201, 461–468. https://doi.org/10.1016/j.solener.2020.03.013 https://doi.org/.

Jwb, C., Yla, B., Wei, C., Yan, Z., Qcb, C., Htb, C., Yan, W., Xdab, C., 2020. Influence of different-sized inverted-pyramids of silicon texture by Ag manipulation on solar cell performance. Appl. Surf. Sci. 506, 144778 https://doi.org/10.1016/j.apsusc.2019.144778 https://doi.org/.

Richter, A., Benick, J., Feldmann, F., Fell, A., Hermle, M., Glunz, S.W., 2017. N-Type Si solar cells with passivating electron contact: identifying sources for efficiency limitations by wafer thickness and resistivity variation. Sol. Energy Mate. Sol. Cells 173, 96–105. https://doi.org/10.1016/j.solmat.2017.05.042 https://doi.org/.

Cho, S.Y., Kim, T.Y., Sun, P.P., 2019. Recovery of silver from leachate of silicon solar cells by solvent extraction with TOPO. Sep. Purif. Technol. 215, 516–520. https://doi.org/10.1016/j.seppur.2019.01.059 https://doi.org/.

Lee, J.K., Lee, J.S., Ahn, Y.S., Kang, G.H., 2018b. Efficient recovery of silver from crystalline silicon solar cells by controlling the viscosity of electrolyte solvent in an electrochemical process. Appl. Sci. 8, 2131 https://www.mdpi.com/2076-3417/8/11/2131.

PVInfoLink, SPOT price, cited in February 9, 2022. https://www.infolink-group.com/en/solar/spot-price/?k=wafer%20price.

Dias, P., Schmidt, L., Lunardi, M.M., Chang, N.L., Spier, G., Corkish, R., Veit, H., 2021. Comprehensive recycling of silicon photovoltaic modules incorporating organic solvent delamination – technical, environmental and economic analyses, Resources. Resour. Conserv. Recy. 165 https://doi.org/10.1016/j.resconrec.2020.105241 https://doi.org/.